Journal of Materials Chemistry A

Accepted Manuscript

ROYAL SOCIETY OF CHEMISTRY

www.rsc.org/materialsA

Journal Name

ARTICLE

High efficiency aqueous-processed MEH-PPV/CdTe Hybrid solar cells with a PCE of 4.20%

Received 00th January 20xx,
Accepted 00th January 20xx

DOI: 10.1039/x0xx00000x

www.rsc.org/

Fangyuan Liu, Zhaolai Chen, Xiaohang Du, Qingsen Zeng, Tianjiao Ji, Zhongkai Cheng, Gan Jin and Bai Yang*

Due to low cost, environmental friendliness and efficient, aqueous-processed polymer/nanoctrystal hybrid solar cells (HSCs) have attracted much attention in recent years. To promote the development of aqueous-processed HSCs, the design and synthesis of new water soluble conjugated polymers (WSCPs) are required. In this work, aqueous-processed MEH-PPV/CdTe HSCs are firstly fabricated. A PCE of 4.20% is achieved, which is comparable to the oil-processed MEH-PPV/NC HSCs. The water-soluble MEH-PPV precursor could increase the miscibility between polymers and aqueous CdTe NCs, and decrease their phase size. Furthermore, by adjusting MEH-PPV/CdTe ratio and annealing temperature, the nanoscale morphology of MEH-PPV/CdTe HSCs will change, which impacts charge transfer and transport. These results provide an important approach for efficient aqueous-processed MEH-PPV/NC HSCs.

Introduction

Polymer/nanocrystal hybrid solar cells (HSCs) have attracted much attention due to the low cost of conjugated polymers, the high charge carrier mobility of inorganic nanocrystals (NCs).[1-12] Additionally, NCs exhibit an advantage of adjustable photoelectronic properties because of their tunable size.[13] In the last decade, a variety of NCs and conjugated polymers have been investigated for fabricating polymer/NC HSCs.[14-18] However, these inorganic NCs and polymers are usually synthesized and dissolved in organic solvents, such as chlorobenzene, toluene and chloroform, which are toxic and flammable. As an alternative, aqueous-processed HSCs provide an environment-friendly approach for efficient photovoltaic devices.[19-23] Water soluble conjugated polymers (WSCPs) can be applied to fabricate the photovoltaic devices by spin-coating, printing or ink-jet, which are convenient methods for industrial production.[24, 25] In addition, the solubility of WSCPs in highly polar solvents is desirable for constructing multilayer photovoltaic devices in combination with neutral polymers.

The WSCPs are composed of π-conjugated backbones and charged side groups.[26] However, most of their charged groups cannot eliminate after fabricating the HSCs, which would obstruct the carrier transport.[27, 28] An effective solution is to synthesize WSCP precursors, in which charged groups (such as tetrahydrothiophene) would be eliminated after annealing. The HSCs manufactured in this approach have excellent device performance.[29-33] To promote the development of aqueous-processed HSCs, the design and synthesis of WSCPs are required.

As a semiconducting conjugated polymer, poly[2-methoxy-5-(2-ethylhexyloxy)-1,4-phenylenevinylene] (MEH-PPV) is widely used in HSCs.[34-37] Greenham et al. firstly demonstrated polymer/NC HSCs in 1996, in which donor was MEH-PPV.[38] Because the small phase size of CdSe nanodots led to poor charge transport, the power conversion efficiency (PCE) was low. After that, a lot kinds of MEH-PPV/NC HSCs were fabricated. Cao et al. overcame the phase separation problem by choosing pyridine as solvent, and achieved the highest record for MEH-PPV/CdS devices with PCE of 1.17% in 2007.[39] However, the polymer was not able to fully penetrate NCs. Using water soluble polymer precursors and NCs can significantly control the nanoscale morphology.[14] Up to now, aqueous-processed MEH-PPV/NC HSCs have not been fabricated. Therefore, we focus on aqueous-processed MEH-PPV/CdTe HSCs.

In this paper, the water-soluble MEH-PPV precursor is synthesized through Wessling polymerization process and applied to aqueous inverted HSCs. The precursor can increase the miscibility between polymers and aqueous CdTe NCs, and decrease their phase size.[14, 31] After annealing, the interpenetrating network structure is constructed. And the positively side-chain groups of the precursor can be easily eliminated. This approach could effectively prevent the charges of polymer acting as traps. The intimacy also enhanced exciton dissociation and charge transfer. Thus, we can presume that water-soluble MEH-PPV precursor has excellent photovoltaic performance. A PCE of 4.20% is achieved under simulated 100 mW cm^{-2} AM 1.5G illumination. The nanoscale

State Key Laboratory of Supramolecular Structure and Materials, College of Chemistry, Jilin University, Changchun, P. R. China. E-mail: byangchem@jlu.edu.cn; Fax: +86 431 8519 3423; Tel: +86 431 8516 8478

† Electronic Supplementary Information (ESI) available: Details of NMR and mass spectra of sulfonium salt, UPS of MEH-PPV, J-V characteristics of the hole-only device, TGA of MEH-PPV precursor, and size distribution of CdTe in MEH-PPV:CdTe films. See DOI: 10.1039/x0xx00000x

morphology of MEH-PPV/CdTe HSCs which impacts charge transfer and transport is deeply investigated in this article. These results provide an important approach for efficient solution-processed MEH-PPV/NC HSCs. We believe our research can be beneficial to the future works towards highly efficient aqueous-processed HSCs.

Experimental

Materials

Tellurium powder (200 mesh, 99.8%) was purchased from Aldrich. Sodium borohydride ($NaBH_4$, 99%) and cadmium chloride hemi(pentahydrate) ($CdCl_2 \bullet 2.5H_2O$, 99%) were purchased from the Sinopharm Chemical Reagent Co., Ltd. 2-mercaptoethylamine (MA, 98%) was obtained from Acros. 2,5-Bis(chloromethyl)-4-(2-ethylhexyloxy)anisole and tetrahydrothiophene (98%) were obtained from Alfa Aesar. All materials were used as received.

Preparation of MEH-PPV precursor

MEH-PPV precursor was prepared according to the previous report.[40] 1 g 2,5-Bis(chloromethyl)-4-(2-ethylhexyloxy)anisole was reacted with 2 mL tetrahydrothiophene (molar ratio about 1:4) in 20 mL CH_3OH at 50°C for 20 h. The product was purified by concentrating the reaction solution and then precipitating the condensed solution on cold acetone. The obtained product was then dissolved in methanol (0.2 mol·L^{-1}) with an equal amount of NaOH added dropwise at 0 °C under N_2. After that, the polymerization process was maintained for 1 h. The aqueous solution of the polymer precursors were then dialyzed in the refrigerator for one day.

Preparation of CdTe NCs

In a typical synthesis, 0.28 mL NaHTe (2/3 mol·L^{-1}) solution was injected into 12.5 mmol·L^{-1} N_2-saturated $CdCl_2$ solution in the presence of MA in the pH range of 5.70-5.74. The molar ratio of Cd:MA:Te was set as 1:2.4:0.2. The resultant precursor solution was refluxed for 55 min to maintain the growth of CdTe NCs. After that, the NCs solution was concentrated to 8 mL and then centrifugated at 7000 rpm for 5 min after adding isopropanol to remove ligands and superfluous salts. Subsequently, the NCs was dried in a vacuum oven and then dissolved in deionized water to obtain a 120 mg·mL^{-1} solution.

Device fabrication

The ITO was cleaned using chloroform, acetone, isopropanol and ethanol before drying in a N_2 flow. Next, the ITO substrate was immediately coated with the TiO_2 precursor at a speed of 2000 rpm for 10s. Afterwards, the samples were annealed for 20 min at 500 °C in order to convert the TiO_2 precursor into anatase-phase TiO_2. The active layer was fabricated by spin-coating the mixed solution or CdTe NCs solution at a speed of 700 rpm for 1 min. The first layer was annealed for 2 min at 300 °C in the glove box before spin coating the second layer which was annealed for 60 min at 300 °C in the glove box. Finally, a 5 nm MoO_3 film and a 60 nm gold electrode were evaporated through a mask at a pressure below 10^{-5} Torr, leading to an active area of 0.05 cm^2.

Characterization

Thermal gravity analysis (TGA) was studied with a Q500 thermal gravimetric analyzer (American TA Company). UV-visible absorption spectra were obtained using a Shimadzu 3600 UV-visible-NIR spectrophotometer. Fluorescence spectroscopy was performed with a Shimadzu RF-5301 PC spectrophotometer. FT-IR spectra were taken on a Nicolet AVATAR 360 FT-IR spectrophotometer. The energy band value was measured in an integrated ultrahigh vacuum system equipped with multitechnique surface analysis system (VG ESCALAB MK II spectrometer) ultraviolet photoelectron spectroscopy (UPS). UPS was measured with the He (I) (21.2 eV) line using a negative bias voltage applied to the samples in order to shift the spectra from the spectrometer threshold. Atomic force microscopy (AFM) micrographs were recorded in tapping mode with a Nanoscope IIIa scanning probe microscope from Digital Instruments. Transmission electron microscopy (TEM) was conducted using a Hitachi H-800 electron microscope at an acceleration voltage of 200 kV with a CCD camera. Current density versus voltage (J-V) characteristics were measured by a computer-controlled Keithley 2400 source meter measurement system under 100 mW/cm2 illumination with an AM 1.5G filter. External quantum efficiency (EQE) was recorded under illumination of monochromatic light from the halogen tungsten lamp using a monochromator (Newport IQE 200) and detected by a computer-controlled lock-in amplifier. The TA setup consisted of 400 nm pump pulses doubled from 800 nm laser pulses (~100 fs duration, 250 Hz repetition rate) generated from a mode-locked Ti: sapphire laser/amplifier system (Solstice, Spectra-Physics) and broadband white-light probe pulses generated from 2-mm-thick water. The relative polarization of the pump and the probe beams was set to the magic angle. The TA data was collected by a fiber coupled spectrometer connected to a computer. The EIS measurements were conducted from a CHI 660E electrochemical workstation in dark conditions at zero bias voltage with a frequency ranging from 1 Hz to 100 kHz. NMR spectra were recorded on a Bruker AVANCE 500 MHz spectrometer with tetramethylsilane as the internal standard. Mass spectra were recorded on a GC/MS mass spectrometer.

Results and discussion

Synthesis and characterization of MEH-PPV

MEH-PPV precursor was synthesized by 2,5-bis(chloromethyl)-4-(2-ethylhexyloxy)anisole with tetrahydrothiophene (THT) followed by Wessling reaction.[40] The synthetic route is shown in Fig. 1. Sulfonium salt was separated as white solid. Its structure was confirmed by nuclear magnetic resonance (NMR) (Fig. S1) and mass spectrometer (Fig. S2). MEH-PPV precursor was confirmed by NMR (Fig. S3).

For converting MEH-PPV precursor to MEH-PPV, annealing the polymer film is an effective approach. So thermal stability is an important factor to be characterized. The thermal gravimetric analysis (TGA) results of the MEH-PPV precursor

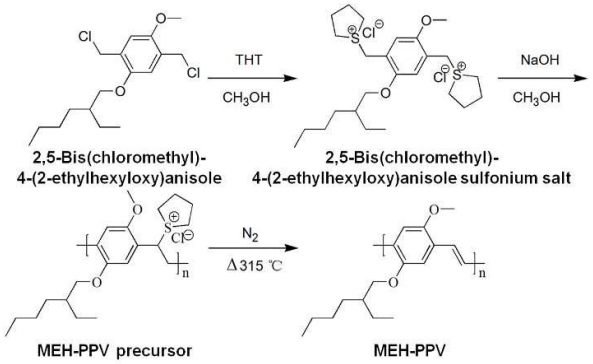

Fig. 1 The synthetic route and chemical structure of MEH-PPV with its precursor.

shown in Fig. 2a illustrate that the chloride ions are removed as hydrogen chloride at temperature higher than 125 °C. Above 220 °C, the THT units begin to be eliminated to form MEH-PPV.[41] The polymer begins to decompose when the temperature is close to 400 °C, and the presence of O_2 also accelerates the decomposition rate. Therefore, we perform the annealing process under vacuum at a temperature between 220-440 °C to prevent thermal degradation and decomposition.

To prove the formation of conjugated structure, the Fourier-transform infrared (FT-IR) spectroscopy measurement is conducted (Fig. 2b). Before annealing MEH-PPV precursor, the characteristic absorption peaks of C=C stretching vibration (1679 cm^{-1}) and vinylene C-H stretching vibration (3047 cm^{-1}) are weak, which means only a little THT is removed. For 60 min at 315 °C, these characteristic absorption peaks are observable enhanced. The normalized X-ray diffraction (XRD) data shown in Fig. 2c has (110) and (210) peaks, which are consistent with literature values from other groups.[42, 43] Before annealing, only the (110) peak can be observed. After annealing, THT is eliminated and carbon-carbon double bonds are constructed. Attributing to higher crystallinity degree and π-π stacking, the (110) peak and (210) peak are strengthened. The UV-Vis absorption and fluorescence peaks of MEH-PPV are 450 nm and 560 nm respectively (Fig. 2d). These results demonstrate the formation of partially ordered conjugated structure and intermolecular π-π interaction.

Fig. 2e represents the atomic force microscopy (AFM) of the MEH-PPV. The corresponding root-mean-square (RMS) roughness is calculated to be 1.568 nm by spin-coating on quartz. The flat surface originates from the polymer nature.

We utilized femtosecond transient absorption technique (TA) to investigate the photoelectric properties of MEH-PPV film. Fig. 2f shows the time-resolved transient absorption spectra recorded at different time intervals after laser excitation at 400 nm. The band from 400 to 620 nm represents the ground state bleaching. And that from 620 to 800 nm is the excited state absorption.[44] Employing ultraviolet photoelectron spectroscopy (UPS) (Fig. S4) and absorption onset, the highest occupied molecular orbital (HOMO) energy level and lowest

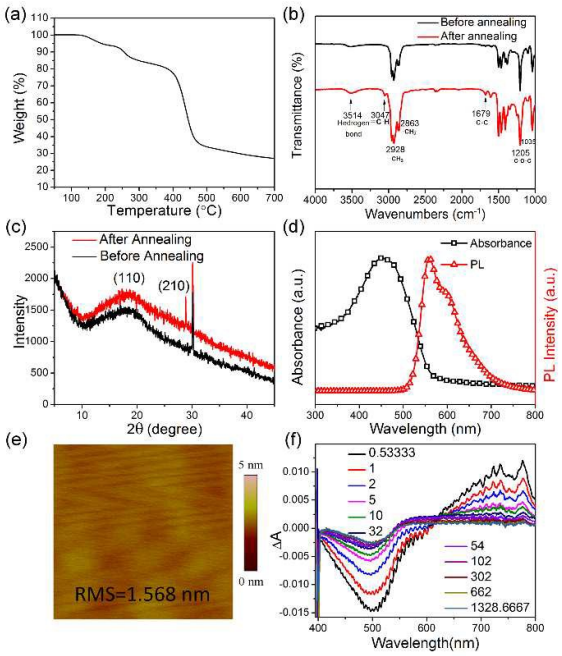

Fig. 2 (a) TGA curve of MEH-PPV precursor. (b) Fourier-transform infrared spectra of MEH-PPV films before and after annealing. (c) X-ray diffraction spectrum of MEH-PPV films before and after annealing. The peak of 29 ° belongs to Si substrate. (d) UV-Vis and fluorescence spectra of the MEH-PPV film on the quartz substrate. (e) AFM image of the MEH-PPV film on the quartz substrate. (f) Transient absorption spectrum of the MEH-PPV film on the quartz substrate excited with the light of 400 nm.

unoccupied molecular orbital (LUMO) energy level are confirmed as -5.22 eV and -3.01 eV respectively. Such high LUMO energy levels are expected to provide enough driving force for efficient exciton dissociation. Besides, the HOMO energy levels are higher than the valence band of CdTe NCs, which ensures the hole transfer from CdTe NCs to the polymers.

The hole mobility of MEH-PPV is measured by the space-charge-limited-current (SCLC) method (Fig. S5a). The devices with configuration of ITO/MEH-PPV/MoO_3/Au were fabricated. The carrier mobility is calculated according to equation (1)

$$J=9\varepsilon_0\varepsilon_r\mu(V-V_{bi}-V_r)^2/8L^3 \quad (1)$$

where ε_0 is the permittivity of free space, ε_r is the dielectric constant of MEH-PPV (assumed as 3), μ is the hole mobility, V is the applied voltage, V_r is the voltage drop due to contact resistance and series resistance across the electrodes, V_{bi} is the built-in voltage, and L is the film thickness. By SCLC method, the hole mobility of MEH-PPV is measured as 3.29×10^{-6} $cm^2V^{-1}s^{-1}$. Compared with the PPV derivatives and poly(2,5-thienylene vinylene) (PTV) derivatives we synthesized before,[29, 30, 33] this hole mobility is low (Fig. S5a-c). PPV and MPPV show higher hole mobility because of stronger intermolecular π-π interaction, which is confirmed by the XRD data (Fig. S6). After annealing at 315 °C, the XRD peak of PPV is strong and sharp while MEH-PPV peak is weak. Long alkoxy side chains of MEH-

Table 1 The optimized device performance parameters of MEH-PPV:CdTe HSCs.

Weight ratio	J_{sc} (mA/cm^2)	V_{oc} (mV)	FF (%)	PCE (%)	R_s (Ω cm^2)	R_{sh} (Ω cm^2)
1:6	11.13 ± 0.44	587 ± 9	50.1 ± 1.6	3.31 ± 0.16	8.55	8150
1:12	13.40 ± 0.16	595 ± 4	50.3 ± 1.4	4.05 ± 0.15	6.00	9600
1:18	14.12 ± 0.36	565 ± 8	50.0 ± 0.2	3.94 ± 0.18	4.72	6400

PPV decreases the planarity and π-π stacking interaction, which lowers the hole mobility. For PTV derivatives, the lone pair electrons of sulphur atom make the electron density of PTV chains higher than PPV derivatives, which lead to higher hole mobility.[33]

Aqueous-processed hybrid solar cells

Hybrid solar cells are fabricated by using our previously reported architecture of ITO/TiO_2/CdTe/MEH-PPV:CdTe/MoO_3/Au (Fig. 3).[29] TiO_2 and MoO_3 are selected as electron transport layer and hole transport layer respectively. A layer of pure CdTe quantum dots (QDs) is cast at the bottom of the polymer:NCs blend film, which can absorb most part of

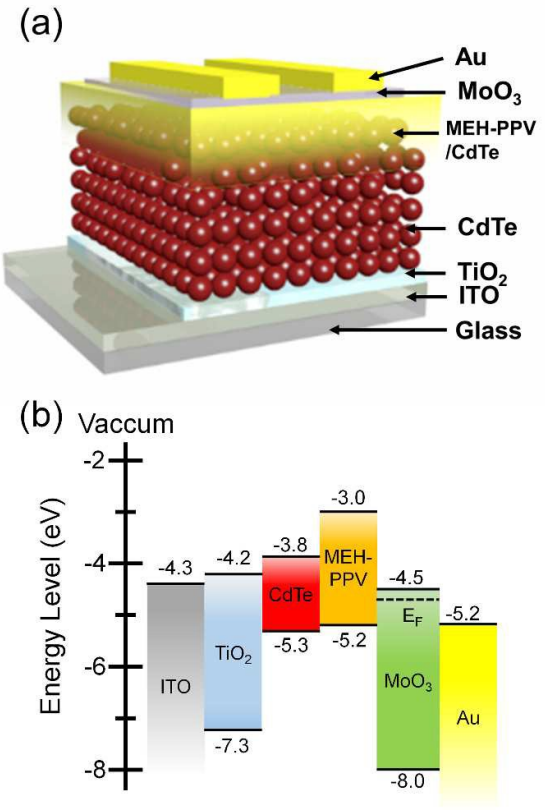

Fig. 3 (a) Device structure and (b) energy level diagram. EF represents Fermi level.

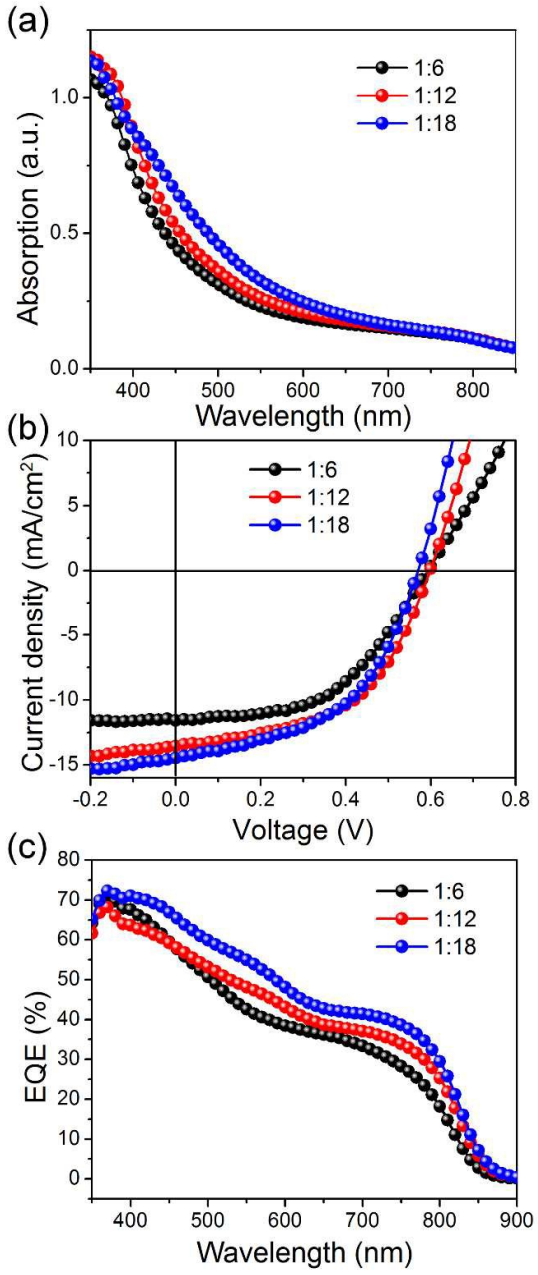

Fig. 4 (a) UV-Vis spectra of different ratio MEH-PPV:CdTe blend films on the quartz substrate. (b) *J-V* characteristics and (c) external quantum efficiency curves of the solar cells with different active layers.

the light. Fig. 4a exhibits the absorption of active layers with different ratios. The absorption increases with the addition of CdTe contents in the hybrid films.

The device performance of the n-i structure is greatly influenced by the MEH-PPV:CdTe weight ratio. Different weight ratios of MEH-PPV:CdTe are studied, including 1:6, 1:12 and 1:18 (Table 1). The current density-voltage curves (*J-V* curves, under AM 1.5G 100 mW cm^{-2}) of the optimized HSCs for each ratio are shown in Fig. 4b, with the detailed photovoltaic parameters listed in the Table 1. The best device with n-i structure shows the PCE of 4.20%, short current density (J_{sc}) of 13.56 mA cm^{-2}, open circuit voltage (V_{oc}) of 0.599 V and fill factor (FF) of 0.517. And when the weight ratio is 1:6, the lower J_{sc} results in a poor device properties. When the ratio is 1:18, although the J_{sc} is 14.48 mA cm^{-2} due to a large content of CdTe, the V_{oc}, FF and PCE are decreased. Because different weight ratio active layers have different morphologies, which will be discussed in detail in the following paragraphs. The corresponding external quantum efficiency (EQE) curve (Fig. 4c) matches well with the increase of J_{sc}. Since light with short wavelength is mainly absorbed by the active layer close to the cathode due to the high absorption coefficient, photogenerated holes need to travel long distance before reaching the anode.

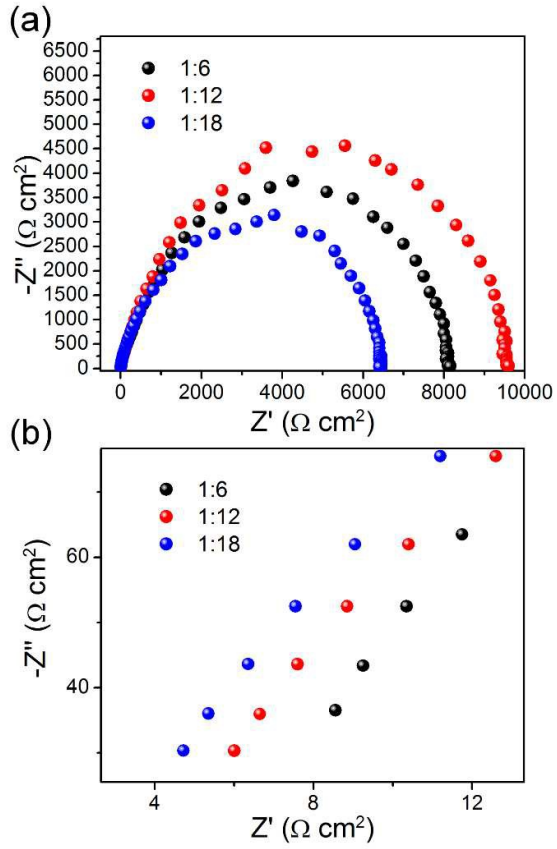

Fig. 5 (a) Electrochemical impedance spectra of the MEH-PPV:CdTe HSCs with different ratio and (b) the high frequency ranges (100-10 kHz) spectra of Fig. 5a.

Electrochemical impedance spectrum (EIS) is utilized to analyze charge dynamics. The EIS measurements were conducted in dark condition with a frequency ranging from 1 Hz to 100 kHz (Fig. 5a). In the measurements, mainly one semicircle was observed on the Nyquist plot for each cell under zero voltage. In high frequency ranges (100-10 kHz) (Fig. 5b), the series resistance (R_s) of 1:6 ratio cell is the highest and the R_s of the 1:18 ratio cell is the lowest. It implies that with the increase of CdTe proportion in active layer, the charge transport resistance decreases and mobility is enhanced. So the short current density is improved. In low frequency ranges (10 kHz-1 Hz), the shunt resistance (R_{sh}) of 1:12 ratio cell is the highest one. This implies the probability of charge recombination is reduced in this optimal device, which is consistent with the improvement of FF and PCE.

Morphology

The morphology of MEH-PPV:CdTe films is an important factor affecting device performance. In order to probe the microscopic change induced by the polymer content, transmission electron microscopy (TEM) is employed to study

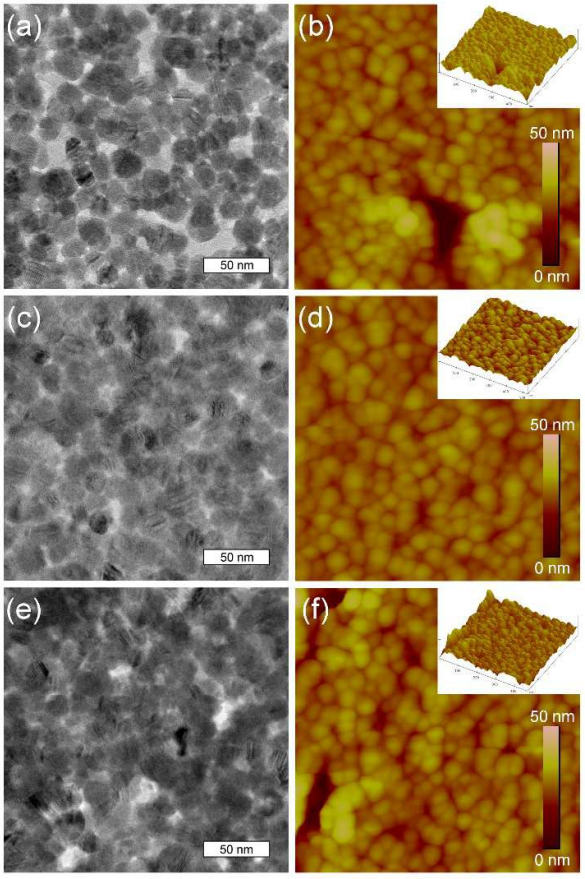

Fig. 6 TEM images and AFM images (500 nm × 500 nm) of MEH-PPV:CdTe blend films with different weight ratio (a), (b) 1:6; (c), (d) 1:12; (e), (f) 1:18. The root-mean-square roughness of blend films are (b) 5.037 nm, (d) 2.488 nm and (f) 4.431 nm.

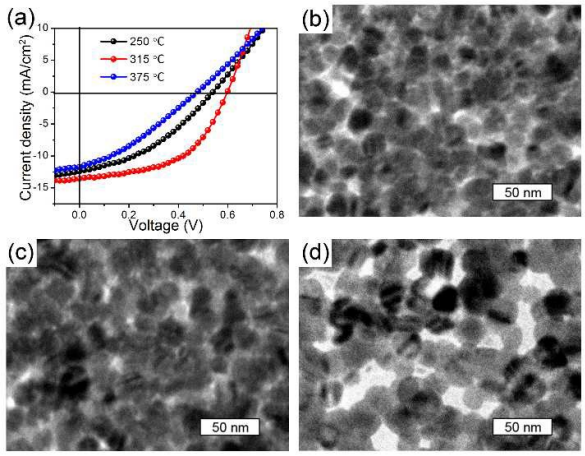

Fig. 7 (a) *J-V* curves of the hybrid solar cells with different annealing temperature. TEM images of MEH-PPV:CdTe films after annealing at (b) 250 °C, (c) 315 °C and (d) 375 °C for 1 h.

the active layer (Fig. 6a, 6c, 6e). When the MEH-PPV:CdTe weight ratio is 1:6 (50 vol-%), CdTe NCs are wrapped by polymer. The nanoparticle phase dimension is too small to form the continuous phase. It causes inferior effect on the electron transport. When the weight ratio is 1:12 (33 vol-%), MEH-PPV percolate through the voids of CdTe NCs, resulting in the optimal photovoltaic performance. CdTe NCs and polymer domains are formed as interpenetrating network structure. This type of bicontinuous percolation network prolong carrier life time. Furthermore, larger donor/acceptor interface improves the exciton dissociation efficiency. At the CdTe loading is 1:18 (25 vol-%), the excessive CdTe NCs in the blend film result in agglomeration. MEH-PPV cannot percolate efficiently in the gap of CdTe-rich domains. Thus, the aggregation of polymers will occur, causing a long distance for hole transport and resulting in a lower PCE. Atomic force microscope (AFM) affords information about the surface topographies of MEH-PPV:CdTe blend films (Fig. 6b, 6d, 6f). By spin-coating and annealing approaches, the minimum root-mean-square (RMS) roughness of blend films is 1:12 weight ratio. The results of TEM images and AFM images are corresponding to each other, which indicate 1:12 is the optimized ratio of MEH-PPV:CdTe.

Annealing temperature is a crucial factor for the thermal stability of polymer and the growth of NCs, which would further impact the charge transfer and transport. We chose 1:12 weight ratio photovoltaic devices for variable temperature experiments. Fig. 7a shows the corresponding photocurrent-voltage curves. We have observed that the devices exhibit poorer performance at 250 °C or 375 °C as compared to at 315 °C. In particular, the fill factor saw a sharp drop in performance level. Further studies with TEM images show substantial distinction of three different annealing temperature active layer (Fig. 7b-7d). For 250 °C annealing, CdTe grains are relative small and dispersed in the polymer. In discontinuous CdTe NCs, charges need to transport multiple times in order to be extracted by TiO_2. When annealing temperature is 315 °C, CdTe NCs combined closely. Meanwhile, MEH-PPV percolate efficiently in the gap of CdTe-rich domains. This kind of interpenetrating network structure makes it possible for the high-efficiency charge carrier to transport. At 375 °C, CdTe NCs grow larger. Meanwhile, as the temperature is too high, polymers decompose to decrease the carrier mobility and leave larger gaps (the decomposition of MEH-PPV was measured by TGA in Fig. S7). Therefore, CdTe phase size is increased. Obvious phase separation leads to leakage current, detrimental recombination and low fill factor. Through experimenting with temperatures, it can be shown that HSCs exhibit best performance at 315 °C.

Compared with oil-phase processed MEH-PPV/NC HSCs, aqueous-processed HSCs successfully overcome the following problem. Oil-phase processed HSCs usually involve mixed organic solvents, which leads to gross phase segregation.[39] In contrast, aqueous process with single solvent is beneficial for achieving appropriate phase segregation, thus increasing the exciton dissociation and charge transport efficiency.

Conclusion

In conclusion, we designed and synthesized specifically the water-soluble MEH-PPV precursors and proved that conjugated polymer can be produced after annealing. An optimized PCE of 4.20% was achieved. We investigated charge dynamics via electrochemical impedance spectra. Furthermore, the ratio of polymer:NCs and annealing temperature can effectively influence the blend films morphology, which is related to the device performance. These results provide an important approach for efficient solution-processed MEH-PPV/NC HSCs. We believe our research can be beneficial to future molecular designs of highly efficient polymer-CdTe aqueous HSCs.

Acknowledgements

This work was financially supported by the National Science Foundation of China (NSFC) under Grant Nos. 51433003, 21221063, 91123031, 51373065, and the National Basic Research Program of China (973 Program) under Grant Nos. 2012CB933800, 2014CB643503.

References

1 W. U. Huynh, J. J. Dittmer and A. P. Alivisatos, *Science*, 2002, **295**, 2425-2427.
2 H. Borchert, *Energy Environ. Sci.*, 2010, **3**, 1682-1694.
3 S. Dowland, T. Lutz, A. Ward, S. P. King, A. Sudlow, M. S. Hill, K. C. Molloy and S. A. Haque, *Adv. Mater.*, 2011, **23**, 2739-2744.
4 H.-L. Yip and A. K.-Y. Jen, *Energy Environ. Sci.*, 2012, **5**, 5994-6011.
5 X. Li, F. Xie, S. Zhang, J. Hou and W. C. Choy, *Light Sci. Appl.*, 2015, **4**, e273.
6 R. Debnath, O. Bakr and E. H. Sargent, *Energy Environ. Sci.*, 2011, **4**, 4870-4881.

7 Q. Zeng, Z. Chen, Y. Zhao, X. Du, F. Liu, G. Jin, F. Dong, H. Zhang and B. Yang, *ACS Appl. Mater. Inter.*, 2015, DOI: 10.1021/acsami.5b07197.
8 K. Dohnalová, A. N. Poddubny, A. A. Prokofiev, W. D. de Boer, C. P. Umesh, J. M. J. Paulusse, H. Zuilhof and T. Gregorkiewicz, *Light Sci. Appl.*, 2013, **2**, e47.
9 M. Wright and A. Uddin, *Sol. Energy Mater. Sol. Cells*, 2012, **107**, 87-111.
10 W. Fu, L. Wang, Y. Zhang, R. Ma, L. Zuo, J. Mai, T.-K. Lau, S. Du, X. Lu, M. Shi, H. Li and H. Chen, *ACS Appl. Mater. Inter.*, 2014, **6**, 19154-19160.
11 W. Fu, L. Wang, J. Ling, H. Li, M. Shi, J. Xue and H. Chen, *Nanoscale*, 2014, **6**, 10545-10550.
12 R. Zhou, R. Stalder, D. Xie, W. Cao, Y. Zheng, Y. Yang, M. Plaisant, P. H. Holloway, K. S. Schanze, J. R. Reynolds, and J. Xue, *ACS Nano*, 2013, **7**, 4846-4854.
13 I. J. Kramer, L. Levina, R. Debnath, D. Zhitomirsky and E. H. Sargent, *Nano lett.*, 2011, **11**, 3701-3706.
14 S. D. Oosterhout, M. M. Wienk, S. S. van Bavel, R. Thiedmann, L. J. A. Koster, J. Gilot, J. Loos, V. Schmidt and R. A. J. Janssen, *Nat. Mater.*, 2009, **8**, 818-824.
15 W. J. E. Beek and R. A. J. Janssen, *Adv. Funct. Mater*., 2002, **12**, 519-525.
16 J. Yang, A. Tang, R. Zhou and J. Xue, *Sol. Energy Mater. Sol. Cells*, 2011, **95**, 476-482.
17 N. Espinosa, R. García-Valverde, A. Urbina and F. C. Krebs, *Sol. Energy Mater. Sol. Cells*, 2011, **95**, 1293-1302.
18 Y. Sun, Z. Liu, J. Yuan, J. Chen, Y. Zhou, X. Huang and W. Ma, *Org. Electron.*, 2015, **24**, 263-271.
19 Q. Qiao and J. T. McLeskey, *Appl. Phys. Lett.*, 2005, **86**, 153501.
20 X. Du, Z. Chen, Z. Li, H. Hao, Q. Zeng, C. Dong and B. Yang, *Adv. Energy Mater.*, 2014, **4**, 1400135.
21 W. Yu, H. Zhang, Z. Fan, J. Zhang, H. Wei, D. Zhou, B. Xu, F. Li, W. Tian and B. Yang, *Energy Environ. Sci.* 2011, **4**, 2831-2834.
22 S. Yao, Z. Chen, F. Li, B. Xu, J. Song, L. Yan, G. Jin, S. Wen, C. Wang, B. Yang and W. Tian, *ACS Appl. Mater. Inter.*, 2015, **7**, 7146-7152.
23 Q. Qiao, L. Su, J. Beck and J. T. McLeskey, *J. Appl. Phys.*, 2005, **98**, 094906.
24 R. Søndergaard, M. Helgesen, M. Jørgensen and F. C. Krebs, *Adv. Energy Mater.*, 2011, **1**, 68-71.
25 T. R. Andersen, T. T. Larsen-Olsen, B. Andreasen, A. P. L. Böttiger, J. E. Carlé, M. Helgesen, E. Bundgaard, K. Norrman, J. W. Andreasen, M. Jørgensen and F. C. Krebs, *ACS Nano*, 2011, **5**, 4188-4196.
26 C. Duan, K. Zhang, C. Zhong, F. Huang and Y. Cao, *Chem. Soc. Rev.*, 2013, **42**, 9071-9104.
27 I. Haeldermans, I. Truijen, K. Vandewal, W. Moons, M. K. V. Bael, J. D. Haen, J. V. Manca and J. Mullens, *Thin Solid Films*, 2008, **516**, 7245-7250.
28 J. Yang, A. Garcia and T.-Q. Nguyen, *Appl. Phys. Lett.*, 2007, **90**, 103514.
29 Z. Chen, H. Zhang, X. Du, X. Cheng, X. Chen, Y. Jiang and B. Yang, *Energy Environ. Sci.*, 2013, **6**, 1597-1603.
30 Z. Chen, F. Liu, Q. Zeng, Z. Cheng, X. Du, G. Jin, H. Zhang and B. Yang, *J. Mater. Chem. A*, 2015, **3**, 10969-10975.
31 Z. Chen, H. Zhang, W. Yu, Z. Li, J. Hou, H. Wei and B. Yang, *Adv. Energy Mater.*, 2013, **3**, 433-437.
32 H. Wei, G. Jin, L. Wang, L. Hao, T. Na, Y. Wang, W. Tian, H. Sun, H. Zhang, H. Wang, H. Zhang and B. Yang, *Adv. Mater.*, 2014, **26**, 3655-3661.
33 H. Wei, H. Zhang, G. Jin, T. Na, G. Zhang, X. Zhang, Y. Wang, H. Sun, W. Tian and B. Yang, *Adv. Funct. Mater.*, 2013, **23**, 4035-4042.
34 S. Kumar and T. Nann, *J. Mater. Res.*, 2004, **19**, 1990-1994.
35 Y. Zhou, Y. Li, H. Zhong, J. Hou, Y. Ding, C. Yang and Y. Li, *Nanotechnology*, 2006, **17**, 4041-4047.
36 S. Zhang, P. W. Cyr, S. A. McDonald, G. Konstantatos and E. H. Sargent, *Appl. Phys. Lett.*, 2005, **87**, 233101.
37 C. Liu, Z. Qiu, F. Li, W. Meng, W. Yue, F. Zhang, Q. Qiao and M. Wang, *Nano Energy*, 2015, **12**, 686-697.
38 N. C. Greenham, X. Peng and A. P. Alivisatos, *Phys. Rev. B.*, 1996, **54**, 17628-17637.
39 L. Wang, Y. Liu, X. Jiang, D. Qin and Y. Cao, *J. Phys. Chem. C*, 2007, **111**, 9538-9542.
40 F. Wudl, P.-M. Allemand, G. Srdanov, Z. Ni and D. McBranch, *ACS Symp. Ser.*, 1991, **455**, 683-686.
41 D. R. Gagnon, J. D. Capistran, F. E. Karasz, R. W. Lenz and S. Antoun, *Polymer*, 1987, **28**, 567-573.
42 R. F. Cossiello, L. Akcelrud and T. D. Z. Atvars, *J. Braz. Chem. Soc.*, 2005, **16**, 74-86.
43 H. V. Shah, J. I. Scheinbeim and G. A. Arbuckle, *J. Polym. Sci., Part B: Polym. Phys.*, 1999, **37**, 605-614.
44 L. Wang, H. Wang, H. Wei, H. Zhang, Q. Chen, H. Xu, W. Han, B. Yang and H. Sun, *Adv. Energy Mater.*, 2014, **4**, 1301882.

The table of contents:

The aqueous-processed MEH-PPV/CdTe hybrid solar cells are firstly fabricated. A PCE of 4.20% is achieved. The nanoscale morphology of MEH-PPV/CdTe HSCs which impacts charge transfer and transport is deeply investigated. It is an important approach for efficient solution-processed MEH-PPV/nanocrystals hybrid solar cells.

Keywords: hybrid solar cells, aqueous process, MEH-PPV, nanocrystals, nanoscale morphology.

Authors: Fangyuan Liu, Zhaolai Chen, Xiaohang Du, Qingsen Zeng, Tianjiao Ji, Zhongkai Cheng, Gan Jin and Bai Yang*

Title: High efficiency aqueous-processed MEH-PPV/CdTe Hybrid solar cells with a PCE of 4.20%

ToC figure: